FEL SIMULATION AND PERFORMANCE STUDIES FOR LCLS-II

G. Marcus, Y. Ding, P. Emma, Z. Huang, T. Raubenheimer, L. Wang, J. Wu
SLAC, Menlo Park, CA 94025, USA

Abstract

The design and performance of the LCLS-II free-electron laser beamlines are presented using start-to-end numerical particle simulations. The particular beamline geometries were chosen to cover a large photon energy tuning range with x-ray pulse length and bandwidth flexibility. Results for self-amplified spontaneous emission and self-seeded operational modes are described in detail for both hard and soft x-ray beamlines in the baseline design.

INTRODUCTION

The LCLS-II is envisioned as an advanced x-ray FEL light source that will be fed by both a superconducting accelerator and the existing LCLS copper linac and will be capable of delivering electron beams at a high repetition rate, up to 1 MHz, to a collection of undulators [1–3]. In the initial phase, referred to as the baseline scenario, the CW linac will feed two independently tuned undulators capable of producing radiation covering a large spectral range with each beamline dedicated to either soft or hard x-ray photon energies. The soft x-ray (SXR) beamline will cover photon energies from $0.2 - 1.3$ keV while the hard x-ray beamline will cover $1.0 - 5.0$ keV. The copper linac will feed the hard x-ray beamline exclusively and will cover photon energies from $1 - 25$ keV. Each of the beamlines will be capable of producing radiation in both the self-amplified spontaneous emission (SASE) and self-seeded (SS) operational modes [4, 5]. While various external seeding and other advanced FEL concepts are being explored for LCLS-II [6, 7], this paper reports the results of detailed FEL simulations in the baseline case for multiple start-to-end (S2E) charge distributions coming from the CW superconducting linac at the higher end of the individual undulator beamline tuning ranges. The simulation code ASTRA [8] was used to track the electron beams through the injector, ELEGANT [9] was used to transport the beams through the linac to the undulators, and GENESIS [10] was used for FEL simulations.

ELECTRON BEAM AND UNDULATOR PARAMETERS

The nominal LCLS-II electron beam and undulator design parameters can be found in Table 1. Both the HXR and SXR beamlines will employ a variable gap hybrid permanent magnet undulator broken into individual segments that are interspersed with strong focusing quadrupoles, adjustable phase shifters, and various other diagnostic elements. The vacuum chamber will be made of Aluminum and will have a rectangular cross section with a full height of 5 mm. The relaxation time for Aluminum is $\tau = 8$ fs and can be used to specify not only the DC but also the AC contributions to the

Table 1: Nominal Electron Beam and Undulator Parameters for the Baseline LCLS-II Scenario

Paramter	Symbol	Value SXR(HXR)	Unit
e-beam energy	E	4.0	GeV
emittance	ϵ	0.45	μm
current	I	1000	A
energy spread	σ_E	500	keV
beta	$\langle \beta \rangle$	12(13)	m
undulator period	λ_u	39(26)	mm
segment length	L_u	3.4	m
break length	L_b	1.0	m
# segments	N_u	21(32)	-
total length	L_{tot}	96(149)	m

resistive wall wakefield (RWW) in the FEL simulations [11]. The SXR beamline is envisioned to operate with a SASE and SS tuning range of $0.2 - 1.3$ keV while the HXR beamline will operate from $1.0 - 5.0$ keV in the SASE mode and will use the electron beam from the copper linac for self-seeding from $5.0 - 12.0$ keV in the baseline case.

The slice parameters of a S2E 100 pC electron beam are illustrated in Figure 1. The core of the bunch, which is roughly 60 fs long, has a very flat phase space with a current of $I \sim 900$A, slice energy spread of $\sigma_E \sim 450$ keV, and slice emittances of $\epsilon_n \sim 0.27$ μm, all of which satisfy the design requirements. It is also relatively well matched to the lattice where the matching parameter $B_{mag} = 1/2 \, (\beta_0 \gamma - 2\alpha_0 \alpha + \gamma_0 \beta) \leq 1.3 - 1.4$ typically does not affect the performance [12, 13].

The slice parameters of a S2E 20 pC electron beam are illustrated in Figure 2. The core of the bunch, which is roughly 30 fs long, has a relatively flat phase space with a current of $I \sim 550$A, slice energy spread of $\sigma_E \sim 280$ keV, and slice emittances of $\epsilon_n \sim 0.1$ μm. The significantly smaller slice emittance and energy spread are extremely beneficial to the performance of the HXR beamline at the high end of the tuning range, as will be illustrated shortly, where the FEL is most sensitive to these parameters. The 20 pC electron beam is also relatively well matched to the lattice with a similar matching parameter in the core of $B_{mag} \leq 1.3 - 1.4$.

The slice energy change over the length of both the HXR and SXR beamlines due to the RWW is illustrated in Figure 3 and Figure 4 for the 100 pC and 20 pC S2E electron beams respectively. It was shown in [14] that the FEL performance could be impacted, due to slowly varying electron beam or undulator parameters, if a slice energy change on the order of $\Delta E \sim 2\rho_{1D}E_0$ occurred before the FEL reached saturation.
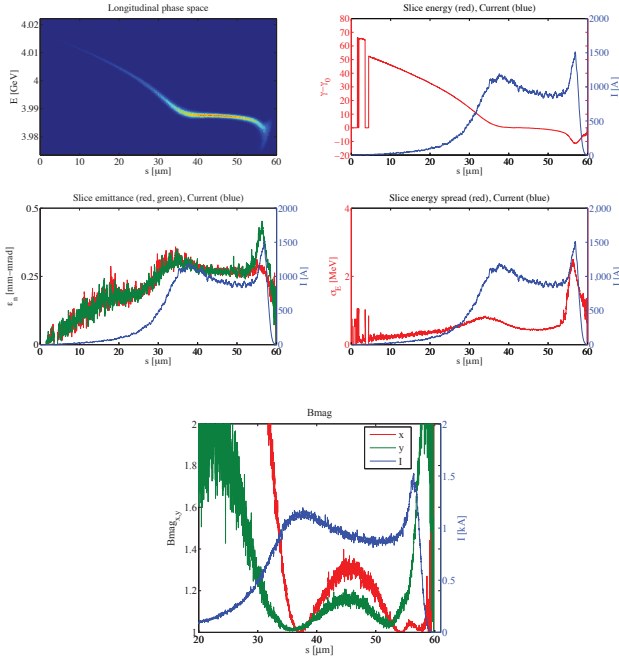
Figure 1: Longitudinal phase space (top left), slice energy (top right), x (green) and y (red) slice nomalized emittance (middle left), slice energy spread (middle right), and matching parameter (bottom) for the 100 pC S2E electron beam. The blue curves are the current and assist in locating the slice properties within the electron beam longitudinal profile.
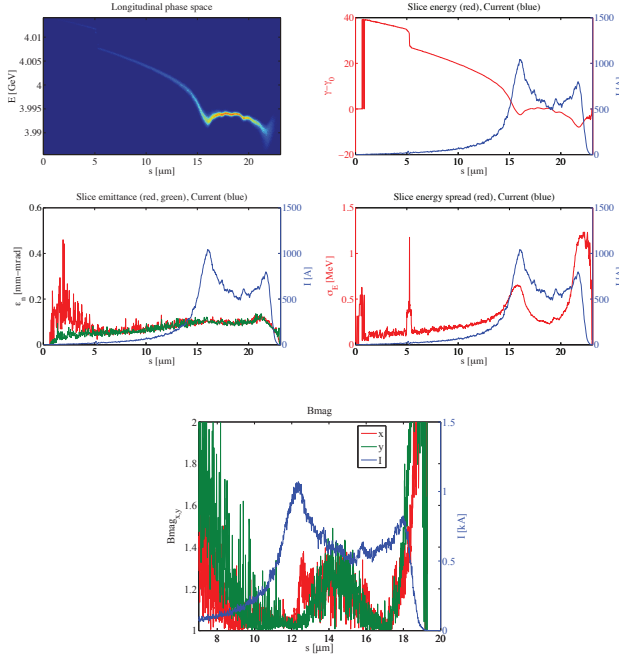

Figure 2: Longitudinal phase space (top left), slice energy (top right), x (green) and y (red) slice normalized emittance (middle left), slice energy spread (middle right), and matching parameter (bottom) for the 20 pC S2E electron beam. The blue curves are the current and assist in locating the slice properties within the electron beam longitudinal profile.
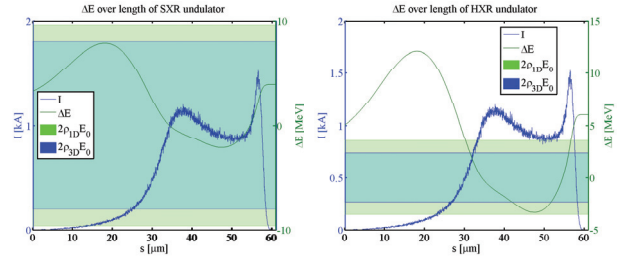

Figure 3: Slice energy change (green line) over the length of the SXR (left) and HXR (right) undulator for the 100 pC electron beam due to the RWW effect. The green (blue) shaded region indicates a tolerable slice energy change with respect to ρ_{1D} (ρ_{3D}) when the undulator is tuned to the higher end of the photon spectral range. The current is shown as the blue line.
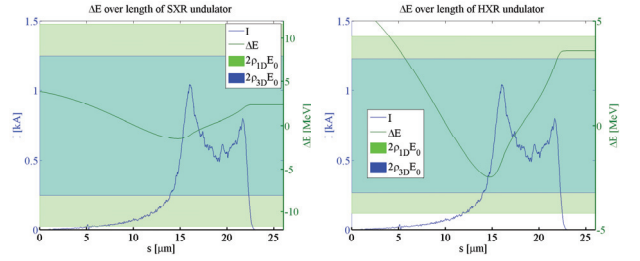

Figure 4: Slice energy change (green line) over the length of the SXR (left) and HXR (right) undulator for the 20 pC electron beam due to the RWW effect. The green (blue) shaded region indicates a tolerable slice energy change with respect to ρ_{1D} (ρ_{3D}) when the undulator is tuned to the higher end of the photon spectral range. The current is shown as the blue line.

Here, ρ_{1D} is the well known FEL Pierce parameter [15] while $\rho_{3D} = \lambda_u/4\pi\sqrt{3}L_g^{3D}$ is an effective FEL parameter defined using the M. Xie formulas [16]. Figure 3 shows that while the SXR beamline is not affected by the RWW in the case of the 100 pC beam, the HXR beamline begins to suffer when the undulator is tuned to produce radiation at the higher end of the tuning range. It can also be seen that the RWW will produce a nonlinear curvature in the LPS of the 100 pC beam, which is often associated with spectral broadening in self-seeding and high-gain harmonic generation operational modes [17]. This particular effect, however, is not noticeable in the SXR beamline as shown below. Moving to a lower charge (and lower peak current) significantly reduces the RWW effect as illustrated in Figure 4, where the energy chirp imparted to the LPS is roughly linear across the beam.

The SXR beamline will incorporate a self-seeding system (SXRSS) to produce longitudinally coherent soft x-ray free electron laser pulses. The HXR beamline will also incorporate a self-seeded beamline. However, it will only operate with the electron beam coming from the copper linac in the baseline scenario, and thus is not presented here.

The SXRSS system consists of two undulators that are separated by a monochromator and a magnetic chicane. The first undulator consists of 7 independent segments while the second undulator consists of 14 independent segments. The monochromator design for the LCLS-II will be based on the existing LCLS SXRSS monochromator [18]. It has a compact footprint that is designed to allow both the chicane and monochromator to occupy the equivalent space of a single undulator segment along the strong focusing quadrupole FODO cell strongback. The resolving power is nominally specified to be $R = 5000$, but upgrade paths to $R \sim 10,000$ are being explored.

The SASE FEL process in the first undulator begins from shot-noise and is interrupted well before saturation in the linear regime. In this way, the slice properties of the electron beam are preserved for an additional FEL process downstream. The SASE FEL x-ray beam is sent through a monochromator which selects a narrow band of the radiation profile while the electron beam passes through the magnetic chicane. The specification of the individual components of both the monochromator and chicane are not yet established. As such, a phenomenological approach is used to model the bandwidth reduction of the seed. The nominal monochromator design relative bandwidth ($1/R$) and overall efficiency (2%) are used to specify the amplitude of a Gaussian filter function. The phase of the filter function is defined through Kramers-Kronig relations such that causality is not violated when the filter is applied to the fully three-dimensional FEL pulse exiting the seventh undulator section. The fields exiting the monochromator are then used to specify the seed into the next undulator. The magnetic chicane serves the dual role of compensating for the delay introduced by the monochromator and destroying any residual electron beam microbunching from the first undulator. This is important because the narrow bandwidth radiation from the monochromator would have a transmitted power much less than the effective power of the microbunching. The monochromatized radiation and the demodulated electron beam then interact in a seeded FEL process in the second undulator where the seed power dominates the electron beam shot noise. The narrow bandwidth (much narrower than the SASE bandwidth) seed radiation is amplified to saturation where the second undulator is tuned such that the seed is at the fundamental resonant frequency.

NUMERICAL SIMULATIONS

We begin with the results of SASE simulations in the SXR beamline tuned to produce radiation at the high end of the tuning range of $E_\gamma = 1.24$ keV or $\lambda_r = 1$ nm using the nominal 100 pC S2E electron beam. As illustrated in Figure 5, saturation is reached after 11 of 21 undulator sections at an energy of $E_{sat} = 220$ μJ. There is significant room to explore post-saturation tapering. The full width at half maximum (FWHM) temporal duration is $\Delta\tau \sim 60$ fs while the relative FWHM bandwidth is $\Delta E_\gamma/E_{0,\gamma} \sim 1.6 \times 10^{-3}$. Operating the SXR beamline without a taper at a repetition rate
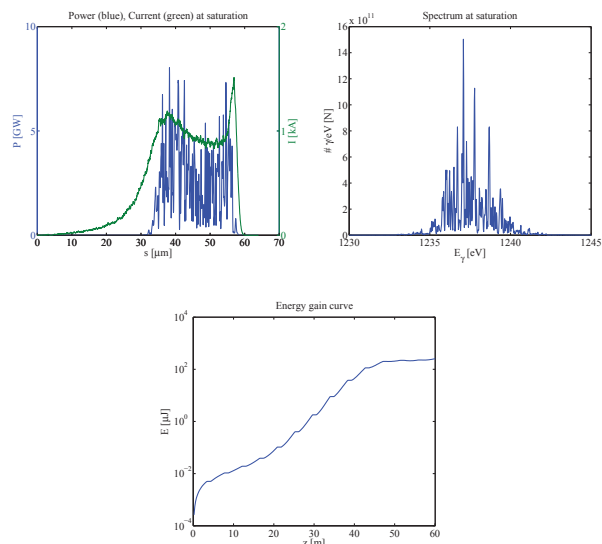

Figure 5: Energy gain curve for SASE FEL simulations using the 100 pC S2E electron beam (bottom). Power profile (blue) and current (green) (top left) and spectrum (top right) at saturation.

of 1 Mhz would deliver ~ 220 W of average power, which is more than the transport optics will be designed to accommodate in the baseline case. Therefore, methods to control this power, for example using electron beam energy chirp control at the undulator or time-dependent bunch manipulation at the injector, while still allowing the FEL to saturate are being explored.

The results for SXRSS simulations where the undulator was again tuned to produce radiation at $E_\gamma = 1.24$ keV is shown in Figure 6 for ten independent runs where only the random number seed for the generation of shot-noise in GENESIS was changed. The FEL pulse amplifies to just over $E = 1$ μJ in the first stage of amplification where single SASE spikes typically reach $10 - 20$ MW. The monochromatized radiation had an average power of ~ 25 kW after the Gaussian filter function was applied, which is much larger than the estimated shot noise power of ~ 500 W. Because the pulse is rather long temporally, the monochromatized field contains a few SASE spikes in the spectral domain, which are amplified to saturation after 16 undulator segments. The pulse energy at saturation is $E_{sat} \sim 200$ μJ. This again leaves room to explore post-saturation tapering. On average (blue curve), however, the relative bandwidth of the SXRSS FEL at saturation approaches the monochromator bandwidth of $\Delta E_\gamma/E_{0,\gamma} \sim 2 \times 10^{-4}$. The bottom right plot of Figure 6 illustrates that there is no bandwidth growth from nonlinear energy curvature induced by the RWW. The red curve is the spectrum from a typical run showing the amplification of a few spikes that make it through the monochromator while the blue curve shows the results of the amplification of a perfectly monochromatic and temporally flat seed and shows very little broadening.
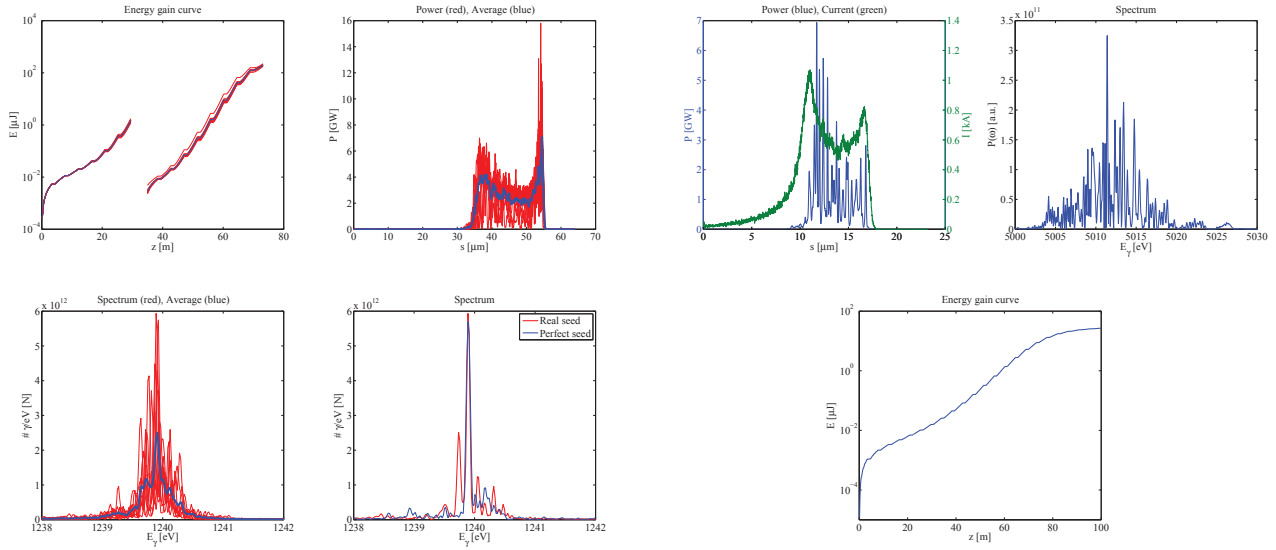
Figure 6: The energy gain curve (top left), power profile (top right) and spectrum (bottom left) for 10 independent runs (red) and their average (blue) using the 100 pC S2E electron beam. The bottom right figure shows the spectrum resulting from the amplification of a perfect seed (blue) and the real seed coming from the monochromator in the second state of the SXRSS beamline.
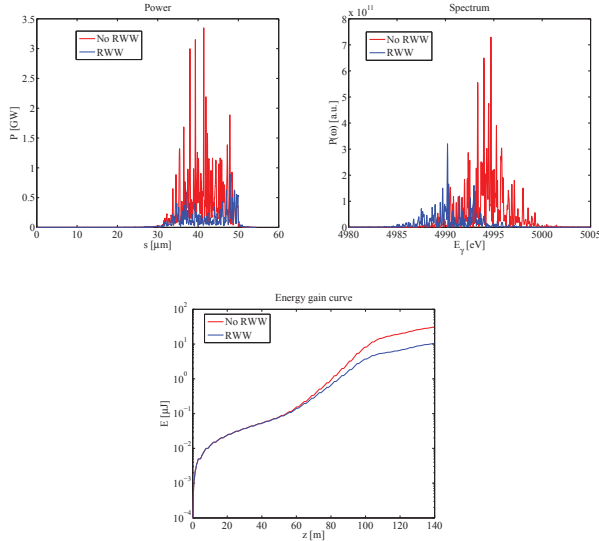

Figure 7: Power profile (top left) and spectrum (top right) at the end of the beamline and the energy gain curve (bottom). Results with the RWW on (off) are shown in blue (red).

The results for SASE simulations in the HXR beamline tuned to produce radiation at the high end of the tuning range of $E_\gamma = 5$ keV using the nominal 100 pC electron beam are shown in Figure 7 with both the RWW turned on in the simulation (blue) and turned off (red). There is a noticeable difference in performance. The RWW suppresses the final energy by about a factor of 3 from $E \sim 30\ \mu J$ (off)
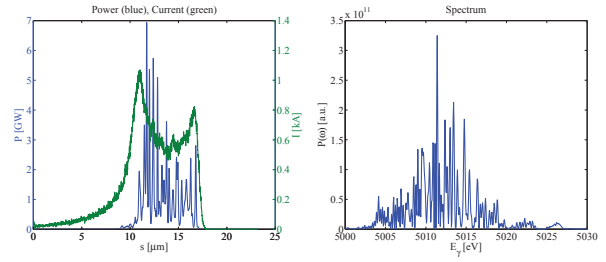

Figure 8: Energy gain curve for SASE FEL simulations using the 20 pC S2E electron beam (bottom). Power profile (blue) and current (green) (top left) and spectrum (top right) at saturation.

to $E \sim 10\ \mu J$ (on), suppresses the amplification of radiation in the core of the beam from spikes that average $P \sim 1$ GW (off) to $P \sim 300$ MW (on) and redshifts the spectrum. There exists, however, some flexibility in tuning a linear taper to slightly mitigate the performance degradation. Either way, the FEL does not seem to reach full saturation by the end of the undulator. This leaves no room for post-saturation tapering and allows for no overhead. Better performance at $E_\gamma = 5$ keV can actually be obtained by going to lower charge where the drastically smaller emittance and smaller energy spread produce a much shorter gain length as illustrated in Figure 8, which shows the results for SASE simulations in the HXR beamline using the 20 pC S2E particle distribution. The FEL in this case reaches saturation after 24 of 32 undulator segments at an energy of $E_{sat} \sim 27\ \mu J$. This leaves significant room for post-saturation tapering. The FWHM temporal duration is $\Delta\tau \sim 20$ fs while the relative FWHM bandwidth is $\Delta E_\gamma / E_{0,\gamma} \sim 7 \times 10^{-4}$.

CONCLUSION

The LCLS-II baseline scenario has been extensively studied using S2E FEL simulations in both the HXR and SXR beamlines and for low and high charge distributions. A small sample of these studies are included here for electron beams coming from the CW superconducting linac to illustrate some of the challenges associated with the design. These include, but are not limited to, RWW effects in the undulator, heat load on the optics (both SXRSS monochromator and transport optics), and FEL power control. Identifying and understanding these challenges will enable the LCLS-II to more effectively deliver photon beams that will certainly push advanced x-ray science to new frontiers.

REFERENCES

[1] T. Raubenheimer *et al.*,"The LCLS-II, a New FEL Facility at SLAC", in *These Proceedings: Proc. 36th Int. Free-Electron Laser Conf., Basel*, 2014, WEB01.

[2] P. Emma *et al.*,"Linear Accelerator Design for the LCLS-II FEL Facility", in *These Proceedings: Proc. 36th Int. Free-Electron Laser Conf.*, Basel, 2014, THP025.

[3] J. Schmerge *et al.*, "The LCLS-II Injector Design", in *These Proceedings: Proc. 36th Int. Free-Electron Laser Conf.*, Basel, 2014, THP042.

[4] J. Feldhaus *et al.*, *Opt. Comm.* **140**, 341 (1997).

[5] G. Geloni *et al.*, *Journ. Mod. Opt.* **58**, 16 (2011).

[6] G. Penn *et al.*, "Laser Seeding Schemes for Soft X-rays at LCLS-II", in *These Proceedings: Proc. 36th Int. Free-Electron Laser Conf.*, Basel, 2014, MOP075.

[7] G. Marcus *et al.*, "Harmonic Lasing Options for LCLS-II", in *These Proceedings: Proc. 36th Int. Free-Electron Laser Conf.*, Basel, 2014, MOP054.

[8] K. Flottmann, ASTRA: A space charge tracking algorithm. User's manual available at `http://www.desy.de/mpyflo/Astra_dokumentation`

[9] M. Borland, Elegant, Advanced Photon Source LS-287, (2000).

[10] S. Reiche, *Nucl. Instr. Meth. Phys. Res. Sec. A* **429**, 243 (1999).

[11] K. Bane *et al.*, SLAC-PUB-10707 (2004).

[12] F.-J. Decker *et al.*, SLAC-PUB-5484 (1991).

[13] T. Raubenheimer *et al.*, SLAC-PUB-95-6850 (1995).

[14] Z. Huang *et al.*, *Phys. Rev. ST. Accel. Beams* **8**, 040702 (2005).

[15] R. Bonifacio *et al.*, *Opt. Comm.* **50**, 373 (1984).

[16] M. Xie, *Nucl. Instrum. Methods Phys. Res. Sect. A* **445**, 59 (2000).

[17] A. Marinelli *et al.*, *Phys. Rev. ST Accel. Beams* **13**, 070701 (2010).

[18] Y. Feng *et al.*, "System Design for Self-Seeded the LCLS at Soft X-ray Energies", in *Proc. 34th Int. Free-Electron Laser Conf.*, Nara, 2012, TUoBI01.